Atmospheric
Measurement
Techniques

Supplement of

A comprehensive evaluation of enhanced temperature influence on gas and aerosol chemistry in the lamp-enclosed oxidation flow reactor (OFR) system

Tianle Pan et al.

Correspondence to: Weiwei Hu (weiweihu@gig.ac.cn)

S1 Supply power for Light Source and BHK lamps

For the UV lamps from Light Source Inc., the supply power (8.9 W) was calculated as 185 mA/425 mA × 21 W, where 185 mA is the measured current controlled by the ballast at 10 VAC (full) output; 425 mA and 21 W are the manufacturer specified current and power. For BHK lamps, the supply power (6.3 W) was measured directly with a Kill-A-Watt sensor on the outlet of the lamp controller box at full AC output.

S2 Calculation of the heating energy in OFR

For the temperature measured for a lamp control voltage of 10 V (full AC power) and flow rate of 5 L min^{-1} (Fig. 4), we calculated the fraction of heating energy transferred from the UV lamps to the gas inside the OFR (f_g), the N_2 purge gas (f_{N_2}), and the OFR tube wall (f_s). Results were estimated on the assumption that all the electrical input power of the lamps was finally converted into heat, which led to the rise in temperature. We did not consider the heat exchange between the gas inside the OFR, N_2 purge gas, and OFR surface. The energy of gas inside the OFR (or N_2 inside the lamp sleeves) would be lost due to the gas (or N_2) entering and leaving the OFR (or lamps sleeve), depending on the flow rate and the temperature of the ambient gas (or N_2,0.2 and 20 L min^{-1}). Also, the OFR surface dissipate heat to the ambient air. Based on the timeseries of measured temperature in Fig. 4, the f_g, f_s, and f_{N_2} could be calculated as follows:

$$f_g = \frac{Q_g}{Q_{Total}} = \frac{C_g \times M_g \times \Delta T_{i-(i-1)} + C_g \times m_g \times \Delta T_{i-a}}{Q_{Total}} \qquad (1)$$

$$f_s = \frac{Q_s}{Q_{Total}} = \frac{C_s \times M_s \times \Delta T_{j-(j-1)} + F \times A \times \Delta T_{j-a}}{Q_{Total}} \qquad (2)$$

$$f_{N_2} = \frac{Q_{N_2}}{Q_{Total}} = \frac{C_{N_2} \times M_{N_2} \times \Delta T_{k-(k-1)} + C_{N_2} \times m_{N_2} \times \Delta T_{k-a}}{Q_{Total}} \qquad (3)$$

Where Q_g, Q_s, and Q_{N_2} were the energy in 1 second of lamps allocated to the gas inside OFR, surface of OFR and N_2 purge gas, respectively; Q_{Total} is the total energy from 4 lamps in 1 s (35.6 J, 8.9 W for each lamp at full VAC). C_g, C_s and C_{N_2} were the specific heat capacity of gas (1.005 kJ kg^{-1} K^{-1} at 300 K), OFR surface (aluminium, 0.879 kJ kg^{-1} K^{-1} at 293 K) and N_2 (1.038 kJ kg^{-1} K^{-1} at 298 K); M_g, M_s and M_{N_2} were the mass of gas inside OFR, OFR surface, and N_2 in lamp sleeves; $\Delta T_{i-(i-1)}$ was the temperature difference between ith and (i-1)th second for gas inside OFR. $\Delta T_{j-(j-1)}$ and $\Delta T_{k-(k-1)}$ were similar, for the temperature of OFR surface and N_2 purge gas; m_g was the mass of gas entered or left OFR in one second; ΔT_{i-a} was the temperature difference between the gas left OFR at ith second and ambient air; F was the Heat dissipation area for OFR surface; A was the heat transfer coefficient (3.48 J m^{-2} s^{-1} K^{-1}) and ΔT_{j-a} was the temperature difference between the OFR surface at jth second and ambient air; m_{N_2} was the mass entered or left lamps sleeve in one second; ΔT_{k-a} was the temperature difference between the N_2 left lamps sleeve at kth second and ambient air. Results were shown in Fig. S8.

S3 Calculation of the Richardson number

The Richardson number, a dimensionless number that represents the ratio of buoyancy term to flow shear term, can be calculated as follow (Holman, 2010; Huang et al., 2017):

$$R_i = \frac{g\beta D^3 \Delta T / \nu^2}{(\rho U_{avg} D / \mu)^2} \sim \frac{gD}{T U_{avg}^2} \Delta T \qquad (4)$$

where g is the gravitational acceleration (9.78 m s^{-2}), β is the thermal expansion coefficient of air (T^{-1} for ideal gases), D is the diameter of the flow tube (202 mm), T is the temperature at centerline (39 °C), ΔT is the temperature difference between the centerline and tube wall (4 °C), ν is the kinematic viscosity of air (m^2 s^{-1}), ρ is the density of air (kg m^{-3}), U_{avg} is the average velocity on the cross-section of the flow tube (m s^{-1}), calculated based on the flow rate (5 L min^{-1}) and D, μ is the dynamic viscosity (N s m^{-2}). When Ri<0.1, the natural convection is negligible; when Ri>10, the forced convection is negligible, and the buoyancy forces may lead to flow bifurcation and recirculation (Huang et al., 2017).

Table S1: Temperature sensors used in temperature measurement.

Temperature sensors	Model	Manufacturer
OFR RH/T sensor	Sensirion SHT21	Sensirion AG
Vaisala	HMT130	Vaisala Inc.
Thermocouple	TM-902C, type K	Shenzhen APUHUA Electronic Technology CO. LTD
CEM	DT-83	Shenzhen EVERBEST machinery industry, CO, LTD.

Table S2: Detailed parameters of OFR temperature experiments.

Exp.	Flow rate (L min⁻¹)	Control Voltage (V)	Lamps [1] (num. of lamps×lamp type)	Mesh screen [2]	OFR sensor Position [3]	Position of Probe within OFR [4]	Temp. of surface	Temp. of exhaust
1	5	5	4 × 185 covered	Back	In backplate	Vertical and horizontal at different depth	/ [5]	/
2	5	10/6/5/4/2 [6]	4 × 185 covered	Back	In backplate	Different depth from the inlet in the center	/	/
3	3/5/7	5	4 × 185 covered	Back	In backplate	Different depth from the inlet in the center	/	/
4	5	10	4 × 185 covered	Back	In backplate	300 mm from the inlet in the center	Measured	/
5	5	10→6→5→4→2→0 [7]	4 ×185 covered	Back	In backplate	300 mm from the inlet in the center	Measured	Measured
6	5	10→6→5→4→2→0	2 ×185 covered	Back	In backplate	300 mm from the inlet in the center	Measured	/
7	5	10→6→5→4→2→0	2 ×185 covered	/	300 mm from inlet	300 mm from the inlet in the center	Measured	Measured
8	5	10→6→5→4→2→0	4 × 185	Back	In backplate	300 mm from the inlet in the center	/	/
9	5	10→6→5→4→2→0	2 × 254	Back	In backplate	300 mm from the inlet in the center	/	/
10	5	10→6→5→4→2→0	4 ×185 covered	Front	300 mm from inlet	/	Measured	Measured
11	5	10→6→5→4→2→0	2 ×185 covered	Front	300 mm from inlet	/	Measured	Measured
12	5	10→2→6→3→5→0	4 ×185 covered	Back	In backplate	300 mm from the inlet in the center	/	/

[1] Three types of lamps were used (Figure S2). '185 covered' transmits both 185 and 254 nm radiation, with 80% surface covered with heat-shrink tubes. Lamps of '185' are the same type as '185 covered', but without covering. The lamp of '254' transmits only 254 nm radiation and is not covered.

[2] Two mesh screens are set inside OFR, one near the inlet (Front) and one near the outlet (Back).

[3] The OFR sensor is set in the backplate by default, as shown in Fig. S1.

[4] Extending the external temperature sensor into OFR from the inlet (so the 'Front' mesh screen must be removed). 4 depths were measured for Exp.1-3 (100, 200, 300, and 400 mm from the inlet, respectively)

[5] '/' means no installation or no measurement.

[6] Only one voltage was used during measurement.

[7] Voltage of one setting cycle, each voltage was set to last for 16 min.

**Table S3: SOM parameters used in this study.**

precursor	VOC surrogate	NOx	m_{frag}	ΔLVP	p_1	p_2	p_3	p_4	HOM yield[1]	reference
dodecane	dodecane	low	2	1.83	0.999	0.001	0.001	0.001		Cappa et al. (2013)
		high	0.2627	1.4629	0.9657	0.0010	0.0020	0.0314		Loza et al. (2014)
α-pinene	α-pinene	low	0.305	1.97	0.419	0.426	0.140	0.014	0.44%	Chhabra et al. (2011)
		high	0.1312	1.9139	0.5991	0.2923	0.1079	0.0007	0.44%	Chhabra et al. (2011)
toluene	toluene	low	1.31	1.77	0.185	0.001	0.002	0.812	0.1%	Zhang et al. (2014)
		high	1.3064	1.4169	0.5634	0.3413	0.0016	0.0937	0.1%	Zhang et al. (2014)
m-xylene	m-xylene	low	1.08	2.05	0.102	0.001	0.878	0.019	1.7%	Ng et al. (2007)
		high	0.0736	1.4601	0.1418	0.2971	0.4571	0.1040	1.7%	Ng et al. (2007)

[1] Values are obtained in Bianchi et al. (2019).

Table S4: The modeled variation of SOA yield per temperature (K). The concentration of organic aerosol seed is 15 µg m^{-3} for all cases. The range of model temperature is 20-40 °C.

precursors	NOx	H_i^{vap} evaporation enthalpy (kJ mol^{-1})			
		Equation[1]	50	100	150
dodecane	high	0.0041-0.0052	0.0019-0.0022	0.0036-0.0050	0.0053-0.0095
	low	0.0062-0.0074	0.0026-0.0029	0.0053-0.0070	0.0078-0.010
α-pinene	high	0.0087-0.0089	0.0037-0.0039	0.0077-0.0088	0.011-0.015
	low	0.011-0.013	0.0041-0.0053	0.0091-0.013	0.01-0.011
toluene	high	0.0060-0.0068	0.0023-0.0026	0.0050-0.0063	0.0075-0.010
	low	0.0083-0.023	0.0044-0.0068	0.0077-0.018	0.0095-0.030
m-xylene	high	0.0049-0.099	0.0025-0.0039	0.0045-0.0094	0.0064-0.016
	low	0.0078-0.018	0.0043-0.0063	0.0073-0.015	0.0091-0.023

60 [1] The equation is taken from Epstein et al. (2010), $H_i^{vap} = -11 \times \log C_{i,ref}^* + 131$.
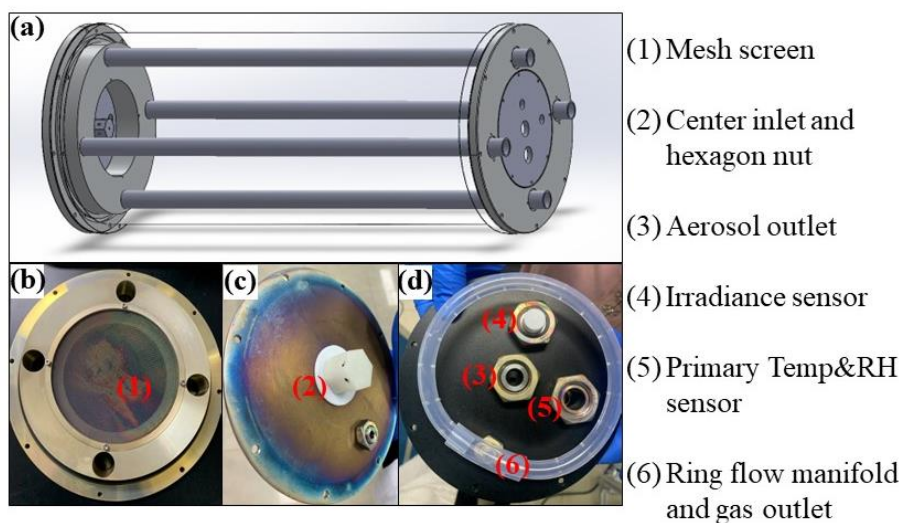
Figure S1: Schematic diagram of (a) OFR and UV lamps and photographs of (b) mesh screen near the inlet, (c) inlet and hexagon nut and (d) outlets and sensors of OFR.
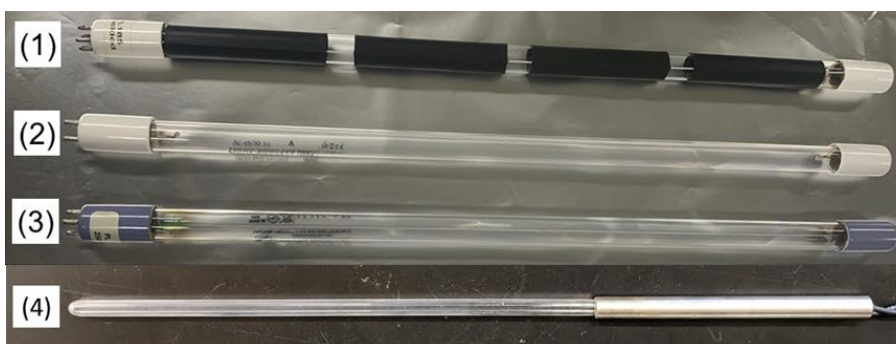
Figure S2: Four types of lamps used in this research. Type (1) transmits both 185 and 254 nm radiation, with 80% surface covered with heat shrink tubes (GPH436T5VH/4, Light Sources, Inc.). Type (2) is the same as type (1) but not covered. Type (3) transmits only 254 nm radiation and is not covered (GPH436T5L/4, Light Sources, Inc.). Type (4) transmits both 185 and 254 nm radiation (model no. 82-9304-03, BHK Inc.).
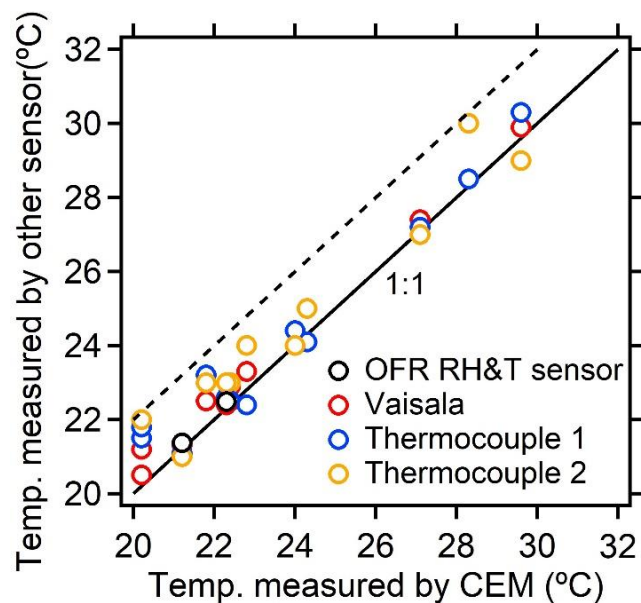
75

Figure S3: Comparison between different temperature measurements used in this research. The measured temperatures from the CEM sensor, which was used to measure the room temperature, are shown on the x-axis. The Vaisala sensor is used to measure the temperature inside the OFR. Thermocouple 1 and Thermocouple 2 are used to measure the temperature of the OFR exhaust and outside surface. Detailed information about different sensors can be found in Table S1.

80
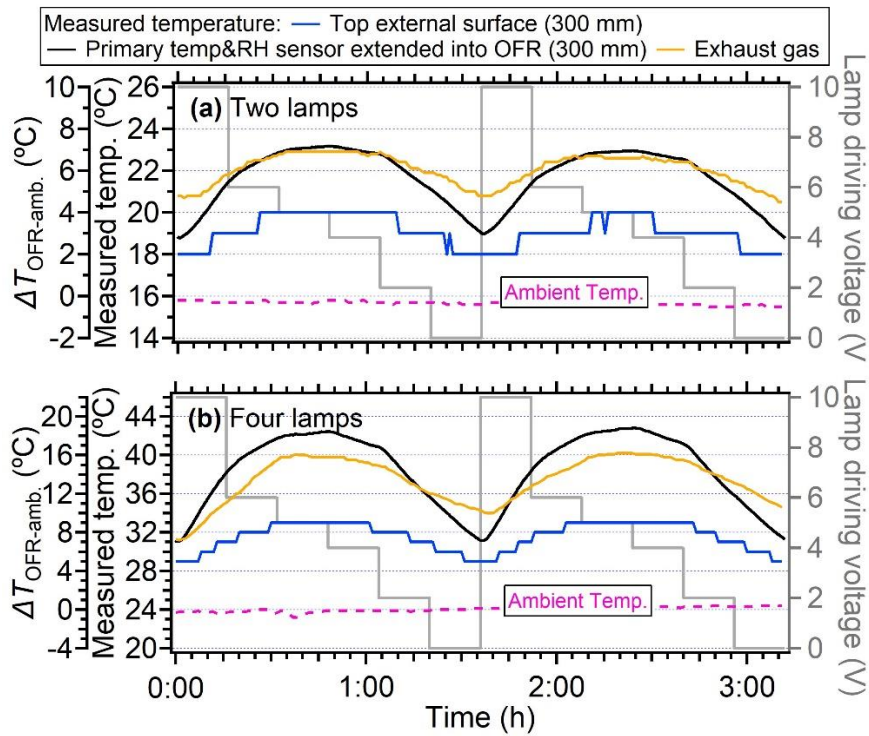
Figure S4: Temperature variation for (a) four lamps and (b) two lamps. In this case, the front plate with a hexagon nut and mesh screen was installed, and the OFR sensor set in the backplate was extended into the center of OFR (probing depth: 300 mm). The mesh screen near the back plate was removed.

85
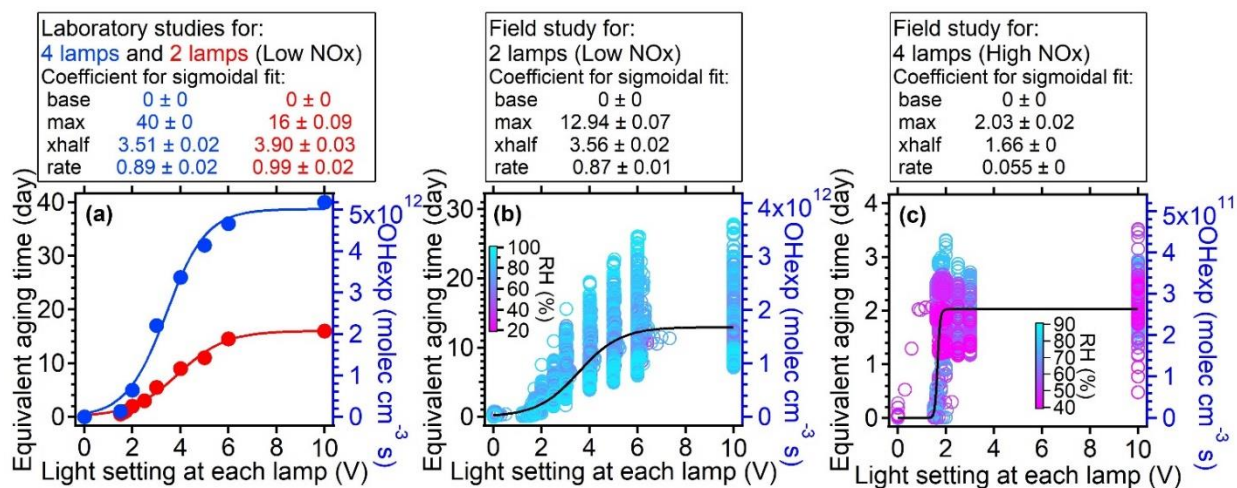
Figure S5: The correlation between OH exposures (right axis) and equivalent aging time (left axis) vs. light settings at each lamp. A sigmoidal function was used to fit the scatter plots. The OH exposures under low NOx condition in panel (a) and (b) were estimated based on the empirical parameterization in Hu et al. (2022), while OH exposures in panel (c) under high NOx conditions was estimated based on the parameterization reported in Peng et al. (2018). A water mixing ratio of 1.88% (60% RH at 25 °C) under low NOx conditions was assumed in the laboratory studies (Panel (a)). The mixing ratio in field studies (Panel (b) and (c)) were measured directly by RH&T sensor. The input flow rate was 5 L min^{-1}, which corresponds to a residence time of 167 s.
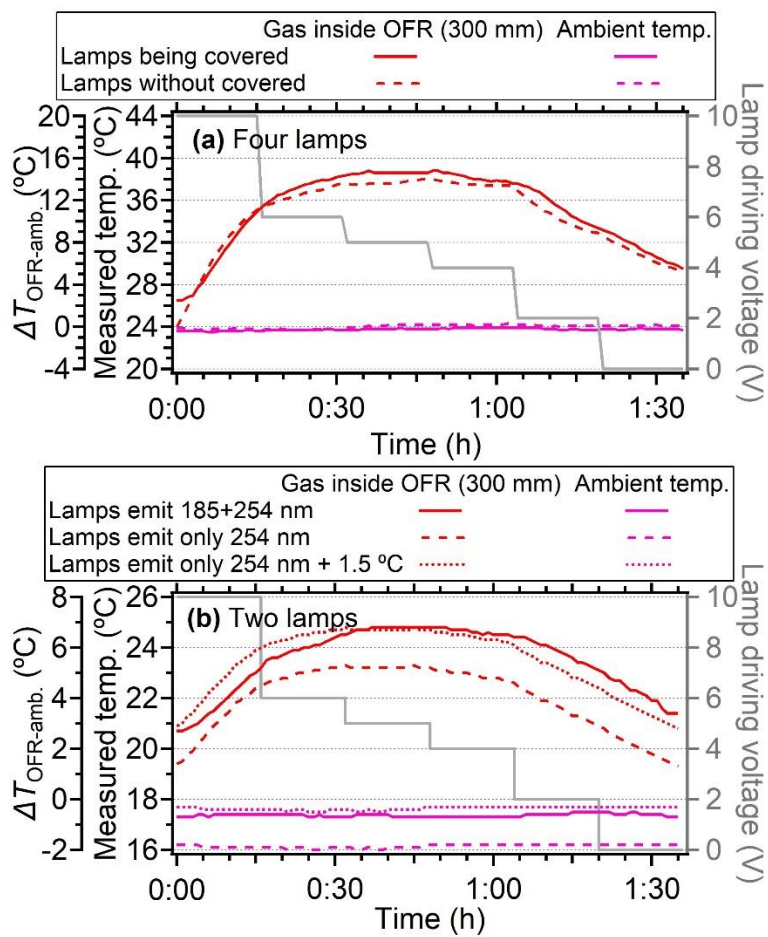
95

Figure S6: The measured temperature variation with different types of Light Source lamps: (a) lamps with 80% surface covered with heat-shrink tubes and lamps without covered, (b) lamps emit both 185 and 254 nm radiation and lamps emit only 254 nm radiation. The temperature of the gas inside OFR at a depth of 300 mm was measured.
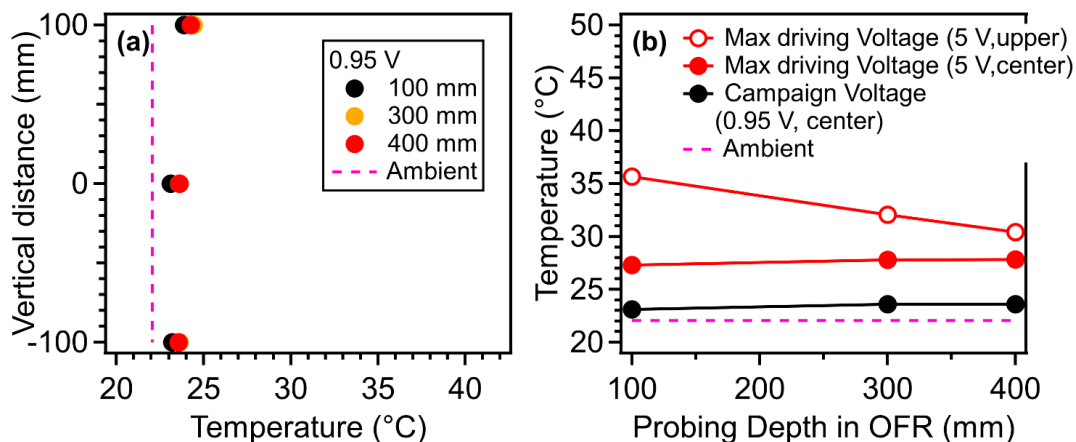
Figure S7: Temperature measured by an external temperature sensor for an OFR with BHK lamps (a) in the vertical direction at different depths inside OFR, with the driving voltage set to 0.95 V for two lamps; (b) the measured temperature at different depths inside the OFR under different driving voltages; the "upper" indicates the position of 100 mm in the vertical direction and the "center" indicated the position measured at centerline. Flow through the OFR was 4.5 L min^{-1}.
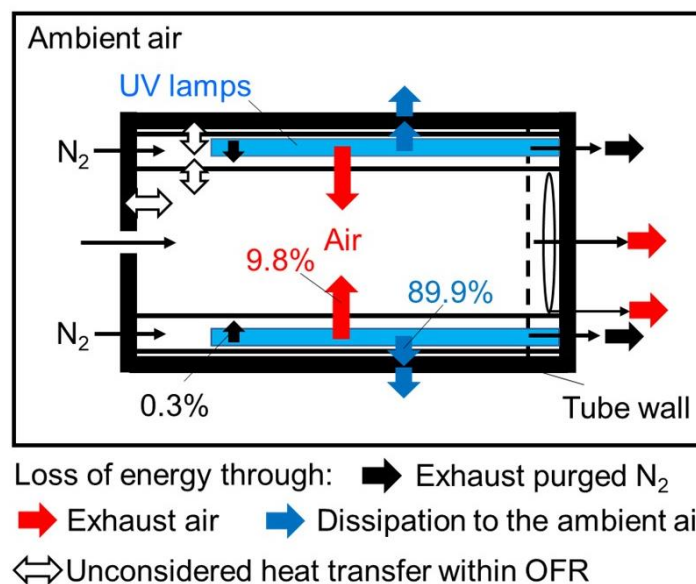

Figure S8: Schematic plot for the transfer of the heating energy inside the OFR from the UV lamps and the loss of energy to the ambient air. The fraction of energy from the UV lamps was obtained from Fig. S9. Note that only the power leading to the temperature increase (51% of total power, which is 35.6 W based on the calculation in Sec S1 and S2) within OFR was considered for these three pathways.

11
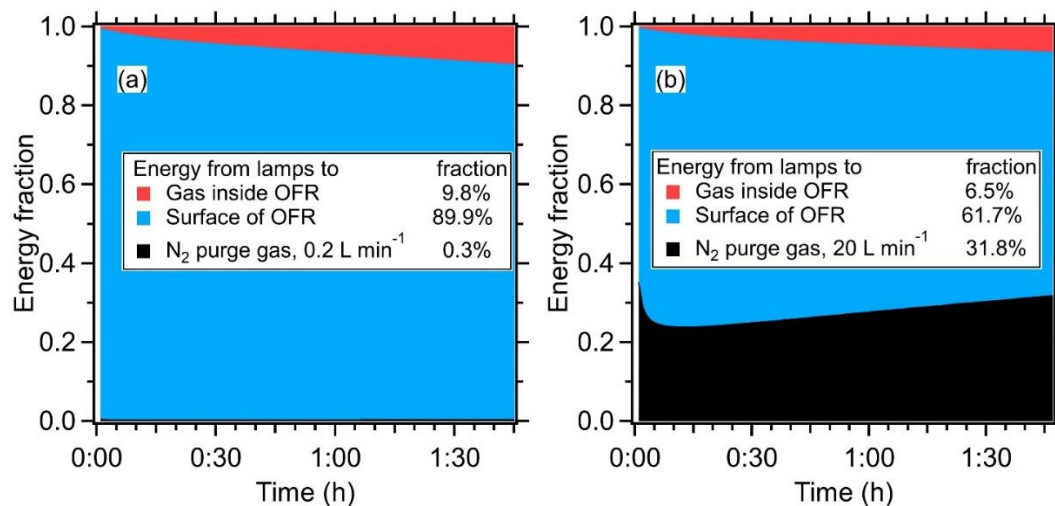
110

Figure S9: (a) Energy from UV lamps (51% (based on calculation in Sect. S2) of total power (35.6 W), 8.9 W for each lamp, 4 lamps in total) to gas inside OFR, surface of OFR and N_2 purge gas (0.2 L min^{-1}) as a function of time, with 4 lamps set to 10 V. The start time was when the lamps were turned on. The flow rate was 5 L min^{-1}. (b) Same as Fig. S9a, with the flow rate of N_2 purge gas increased to 20 L min^{-1}. Details of the energy calculation were presented in Sect. S2.

115
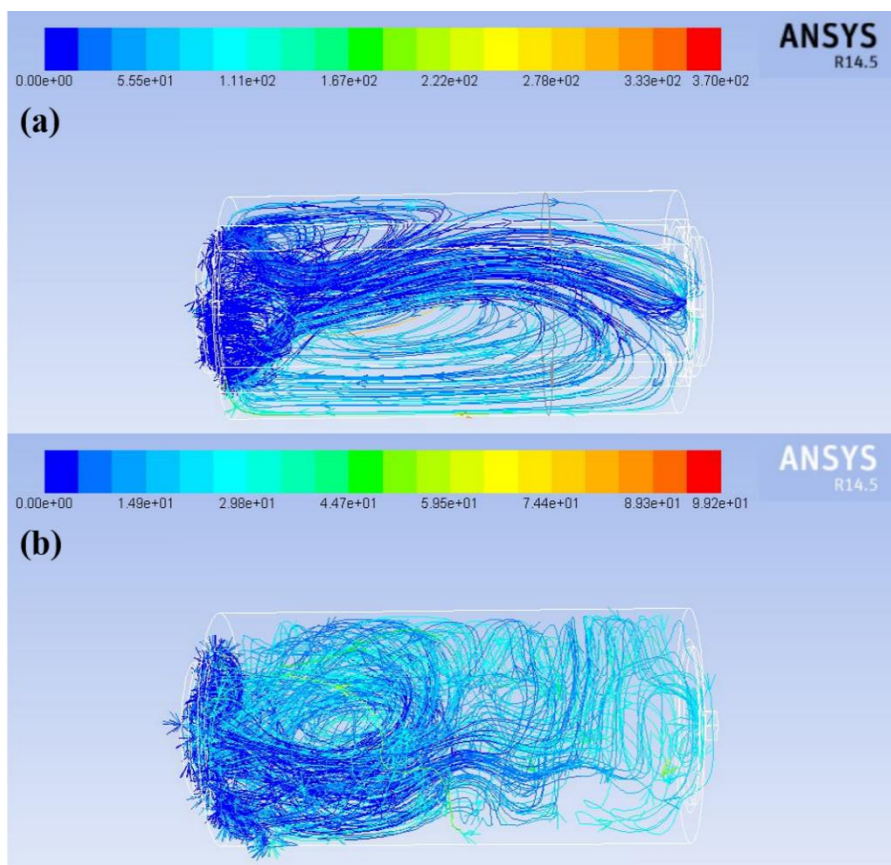
120   **Figure S10: CFD simulation of the gases in OFR (a) without and (b) with the heating of lamps. In panel (b), the scenario of four lamps at 5 V was simulated.**
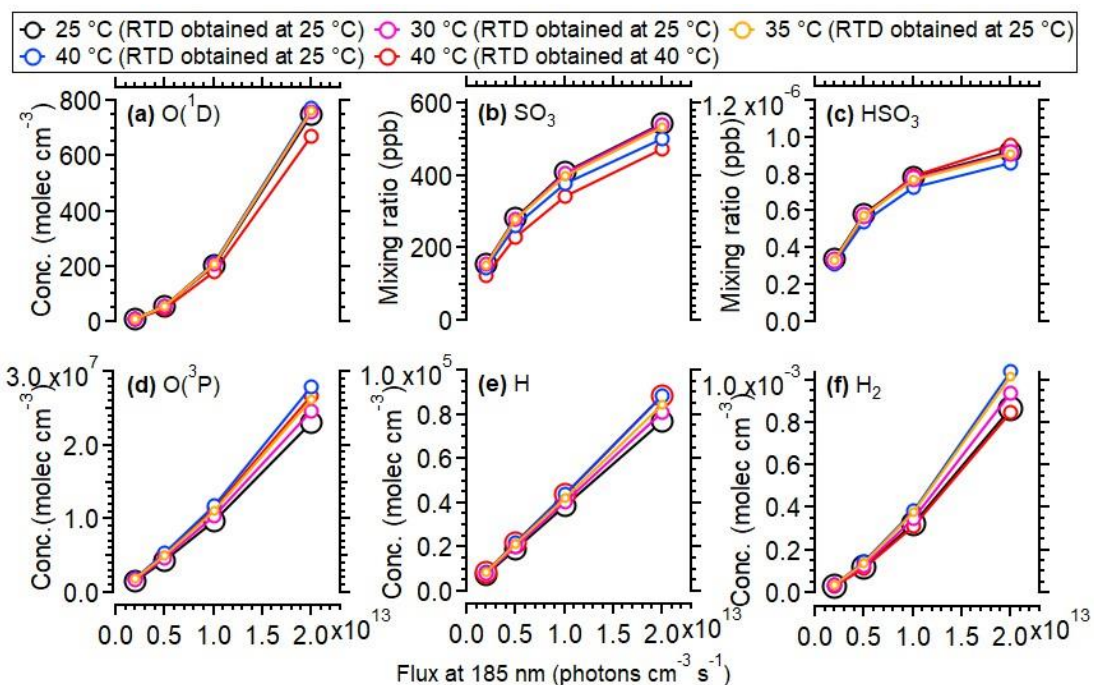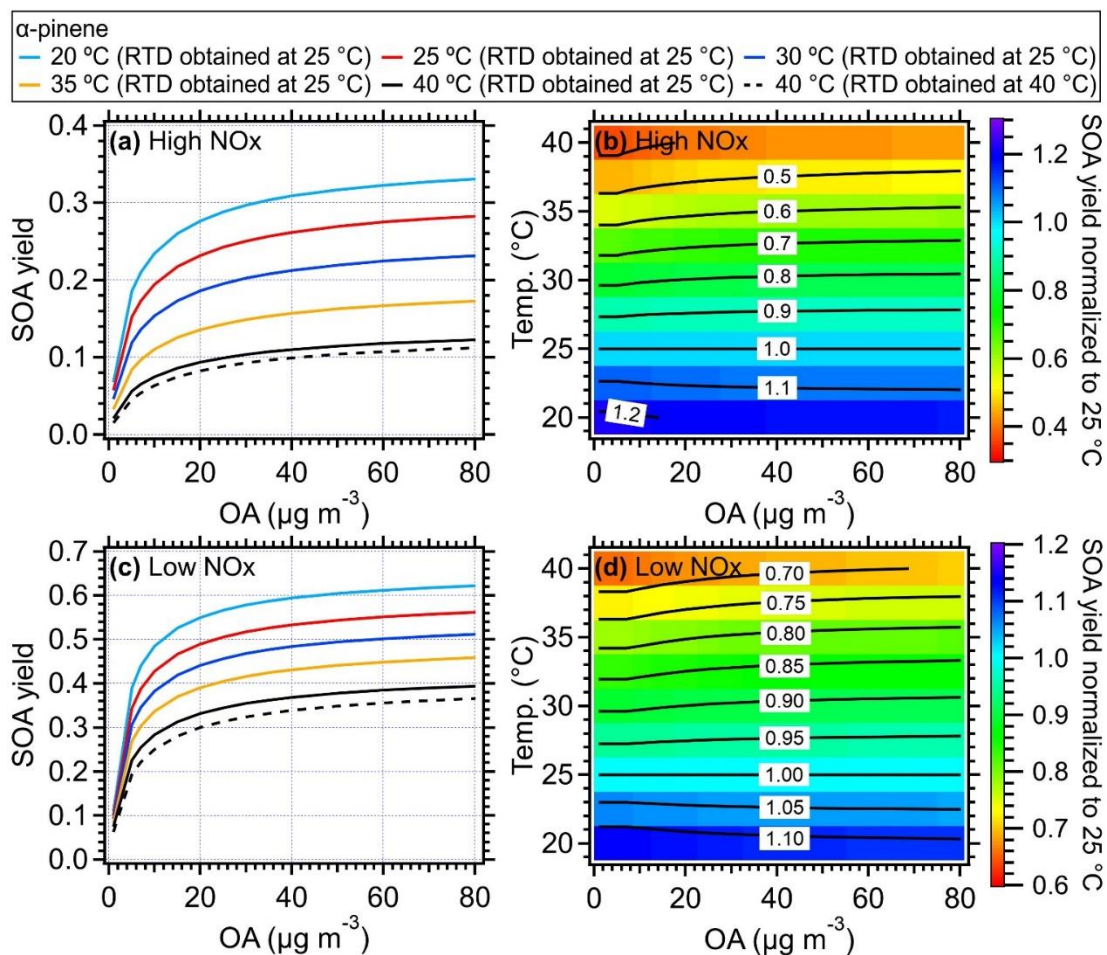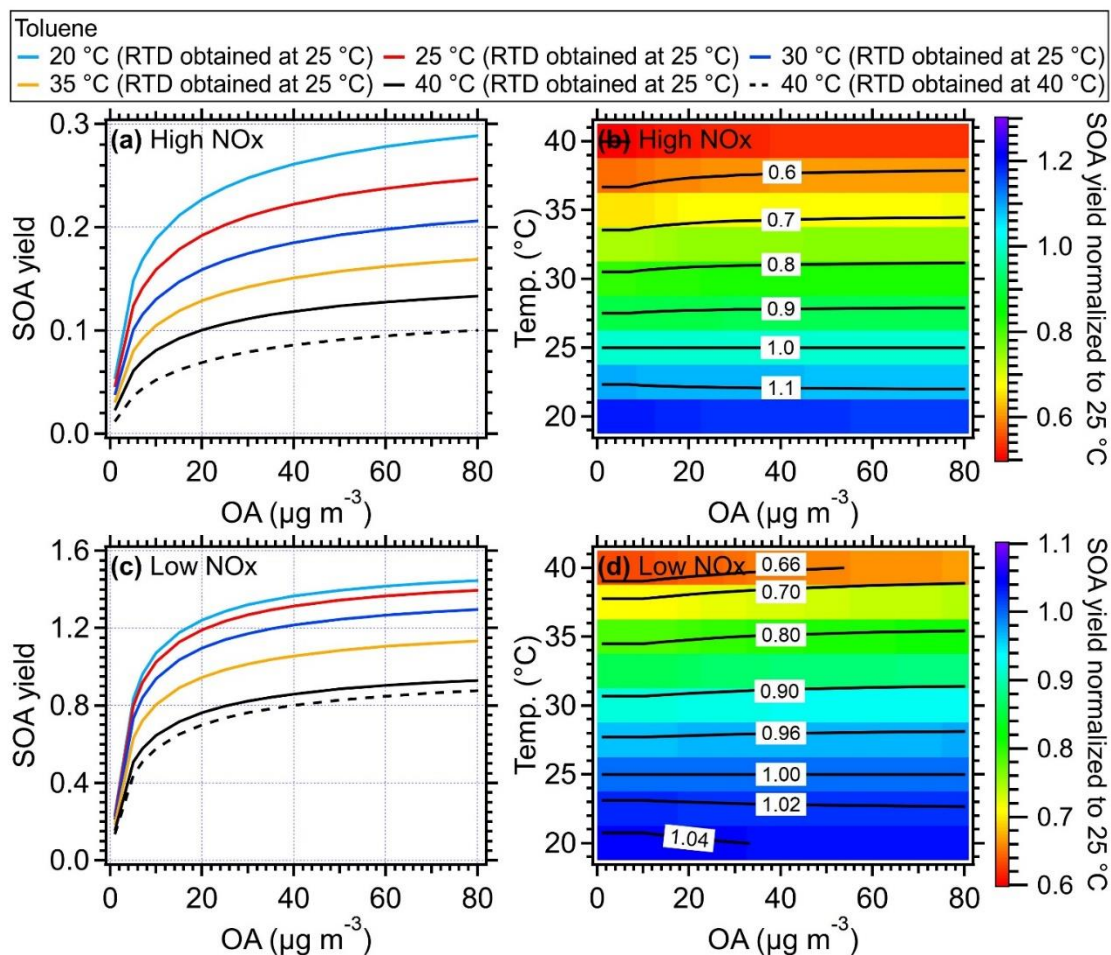
Figure S11: Simulated concentration of oxidant species from 25 to 40 °C in OFR as a function of photon flux at 185 nm. In this scenario, the 800 ppb of initial SO_2, 2.2% water vapor mixing ratio (25 °C, 70% RH), and different photon flux at 185 nm and 254 nm (photon flux ratio of 254/185 nm= 0.05) were used. The simulated oxidant concentrations with measured RTD at 25 and 40 °C were both shown.
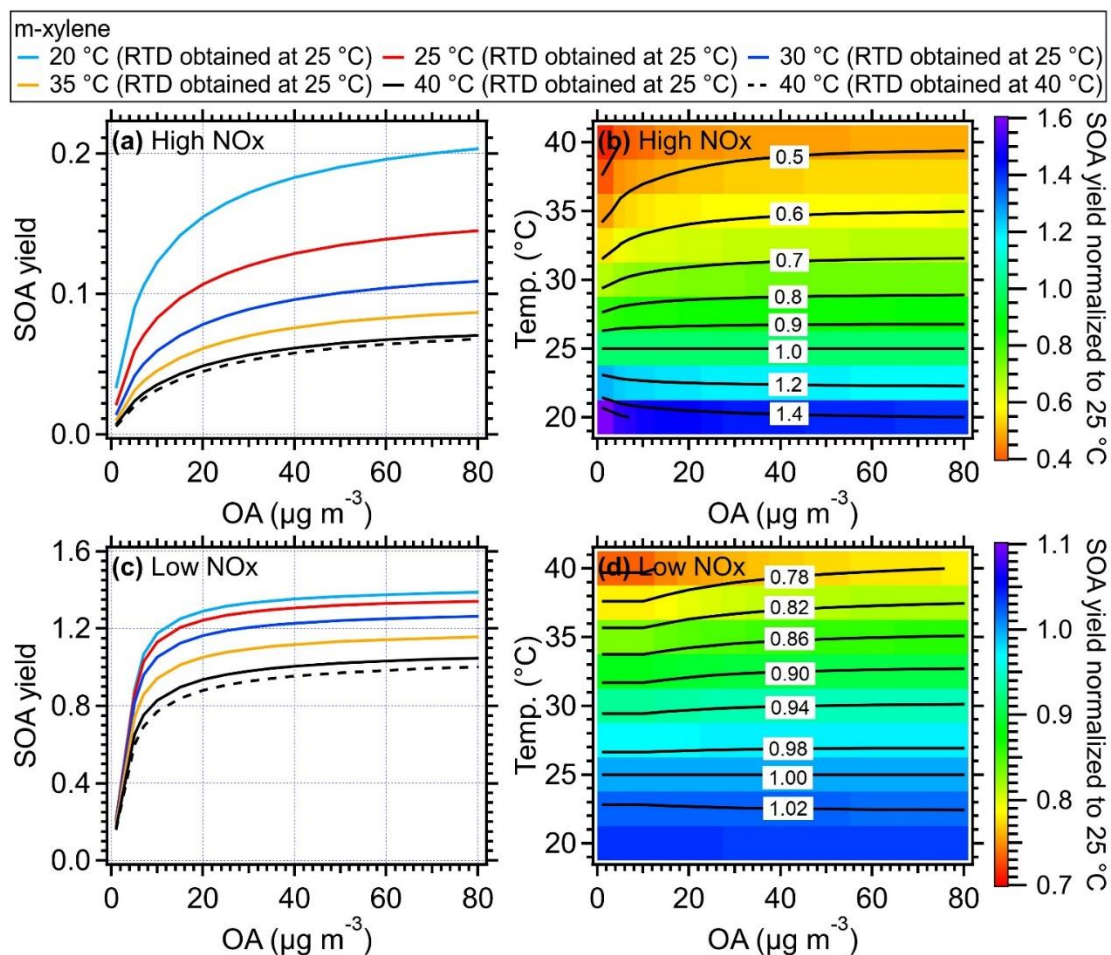
14

Figure S12: Simulated SOA yield of α-pinene as a function of mass concentration of OA seed (inlet mass concentration) and temperature inside of the OFR for (a) high NOx and (c) low NOx conditions, respectively. The simulated results using measured RTD obtained at 40 °C were shown as black dashed lines. The ratio of SOA yield of α-pinene from different temperatures compared to that of 25 °C under (b) high NOx and (d) low NOx conditions. The equivalent aging time was 0.5 days by assuming the ambient OH concentration equated to 1.5×10^6 molecule cm^{-3} (Mao et al., 2009).

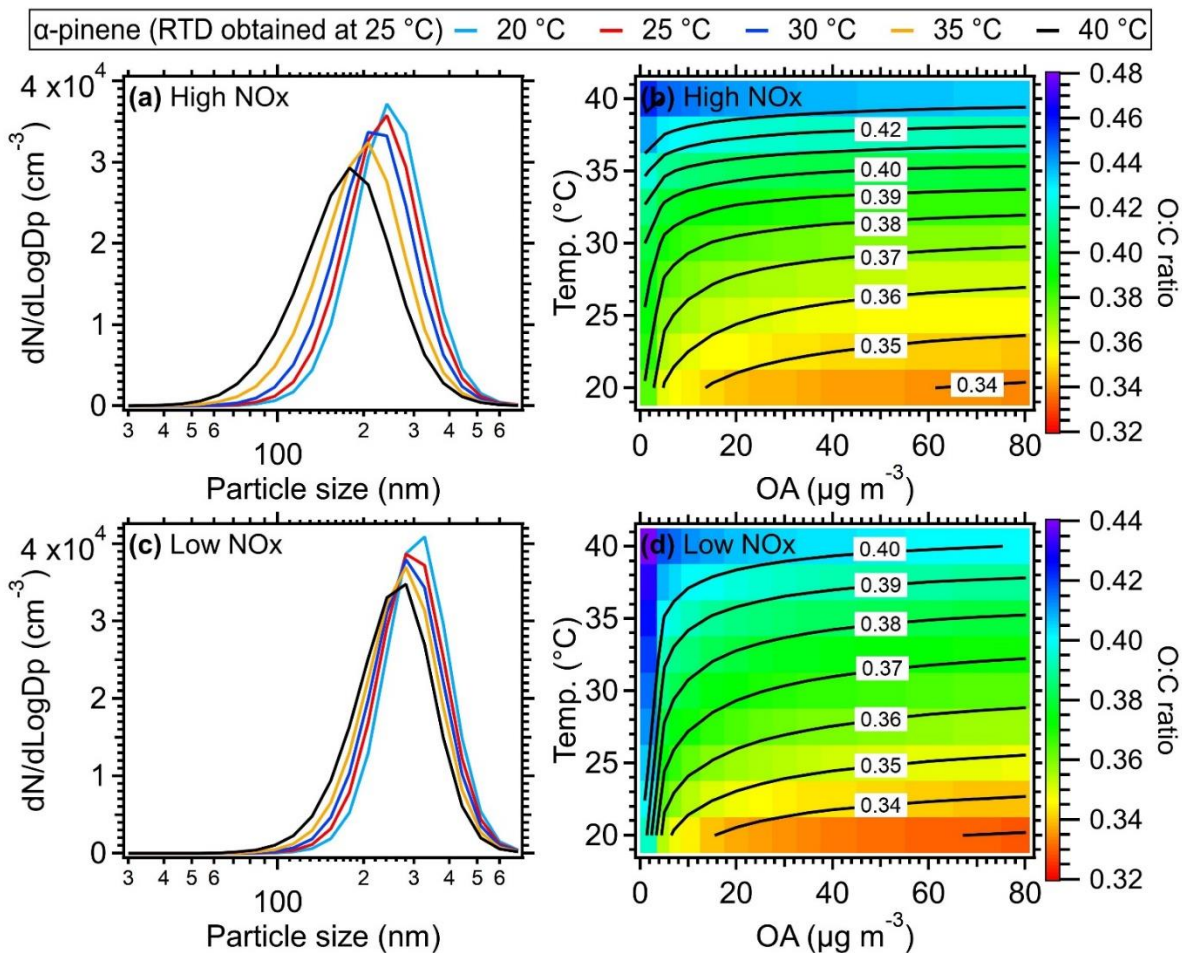135

Figure S13: Simulated SOA yield of toluene as a function of mass concentration of OA seed (inlet mass concentration) and temperature inside of the OFR for (a) high NOx and (c) low NOx conditions, respectively. The simulated results using measured RTD obtained at 40 °C were shown as black dashed lines. The ratio of SOA yield of toluene from different temperatures compared to that of 25 °C under (b) high NOx and (d) low NOx conditions. The equivalent aging time was 1 day by assuming the ambient OH concentration equated to 1.5×10^6 molecule cm^{-3} (Mao et al., 2009).

Figure S14: Simulated SOA yield of xylene as a function of mass concentration of OA seed (inlet mass concentration) and temperature inside of the OFR for (a) high NOx and (c) low NOx conditions, respectively. The simulated results using measured RTD obtained at 40 °C were shown as black dashed lines. The ratio of SOA yield of xylene from different temperatures compared to that of 25 °C under (b) high NOx and (d) low NOx conditions. The equivalent aging time was 1 day by assuming the ambient OH concentration equated to 1.5×10^6 molecule cm^{-3} (Mao et al., 2009).

Figure S15. Simulated size distribution of α-pinene SOA as a function of temperature by assuming the mass concentration of 30 μg m^{-3} for OA seed (inlet mass concentration) under (a) high NOx and (c) low NOx conditions, respectively. Simulated O: C ratio of α-pinene SOA as a function of temperature and mass concentration of OA seed (inlet mass concentration) under (b) high NOx and (d) low NOx conditions. The equivalent aging time was 0.5 days by assuming the ambient OH concentration equated to 1.5×10^6 molec cm^{-3} (Mao et al., 2009).
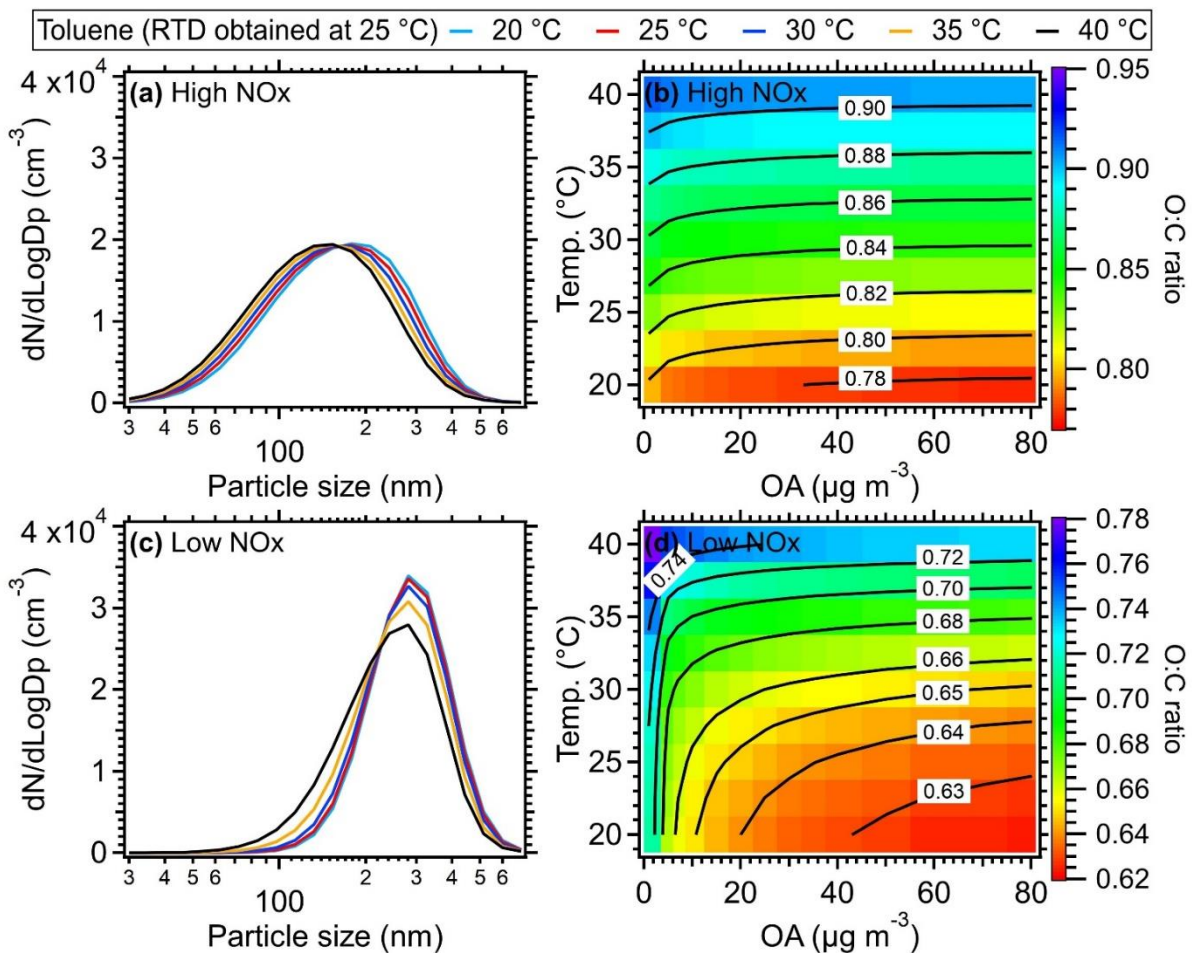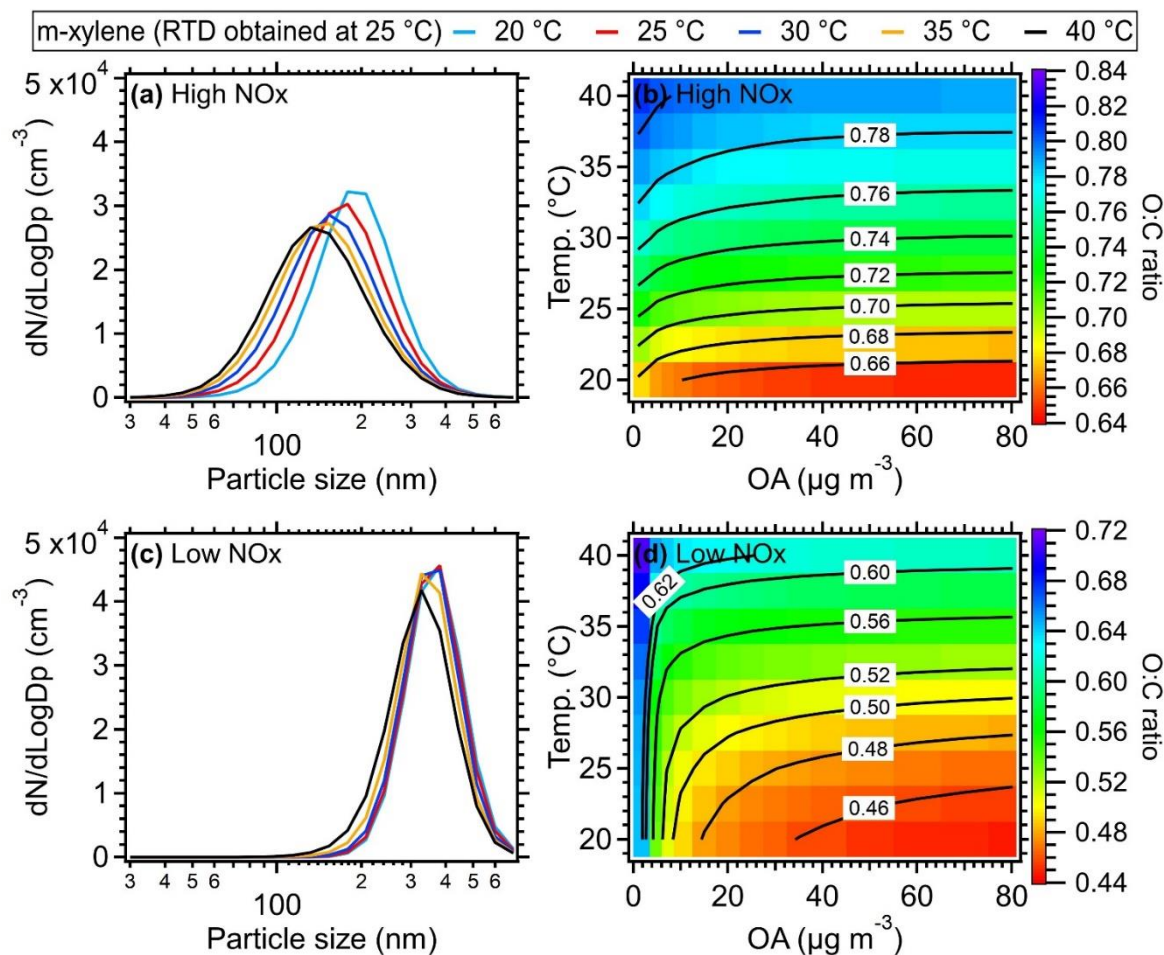
Figure S16: Simulated size distribution of toluene SOA as a function of temperature by assuming the mass concentration of 30 μg m^{-3} for OA seed (inlet mass concentration) under (a) high NOx and (c) low NOx conditions, respectively. Simulated O:C ratio of toluene SOA as a function of temperatures and mass concentration of OA seed (inlet mass concentration) under (b) high NOx and (d) low NOx conditions. The equivalent aging time was 1 day by assuming the ambient OH concentration equated to 1.5×10^6 molecule cm^{-3} (Mao et al., 2009).

Figure S17: Simulated size distribution of m-xylene SOA as a function of temperature by assuming the mass concentration of 30 μg m^{-3} for OA seed (inlet mass concentration) under (a) high NOx and (c) low NOx conditions, respectively. Simulated O:C ratio of m-xylene SOA as a function of temperatures and mass concentration of OA seed (inlet mass concentration) under (b) high NOx and (d) low NOx conditions. The equivalent aging time was 1 day by assuming the ambient OH concentration equated to 1.5×10^6 molecule cm^{-3} (Mao et al., 2009).
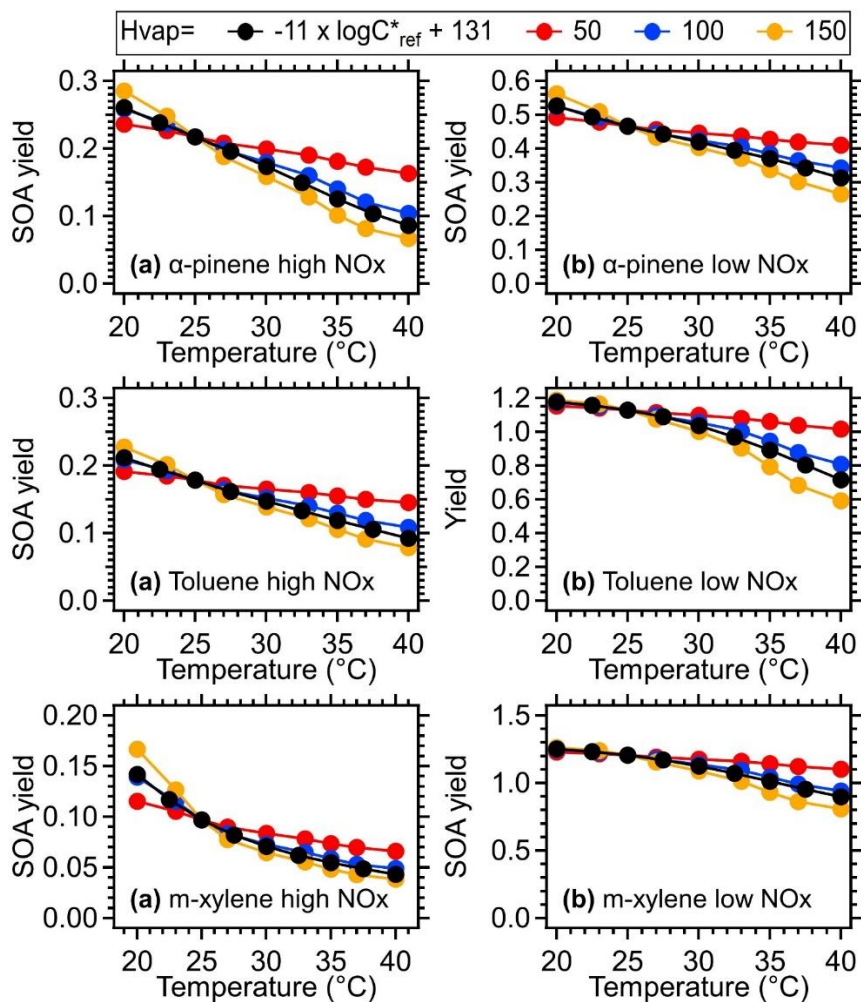
Figure S18: Simulated SOA yield of (a-b) α-pinene, (c-d) Toluene, (e-f) m-xylene as a function of temperature under different H_i^{vap} values (Unit: kJ mol⁻¹). The mass concentration of OA seed (inlet mass concentration) was assumed to be 15 μg m⁻³. The equivalent aging time was 1 day assuming the ambient OH concentration equated to 1.5×10^6 molecule cm⁻³ (Mao et al., 2009).
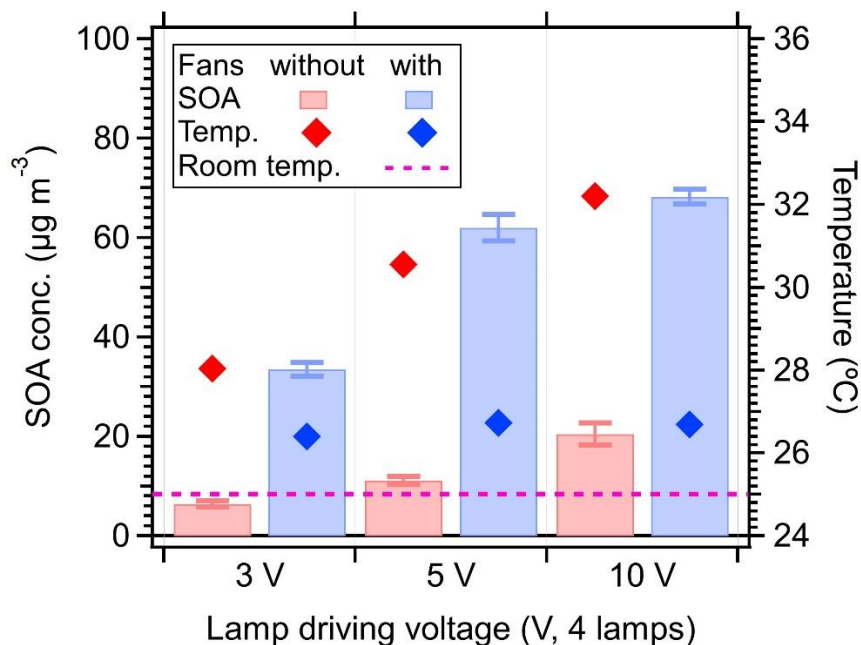
Figure S19. The SOA formation from benzene and OH radicals in the PAM-OFR as a function of light intensity. Two cases including PAM-OFR blown with fans and without fans were both shown. The room temperature and temperature measured with the primary Temp&RH sensor set in the back panel were shown in the right axis. Note
the OFR temperature reported here is the lower limit as discussed in section 3.1.5. The gas-phase benzene (99.80%, Sigma-Aldrich) was generated with syringe pumps. Benzene was used as gas-phase precursor in this experiment due to its lower kOH, since benzene will not be totally consumed under the high OH exposure at high voltage settings in OFR. The flow rate in this experiment was 4.5 L min^{-1}, and the RH was ~30%.
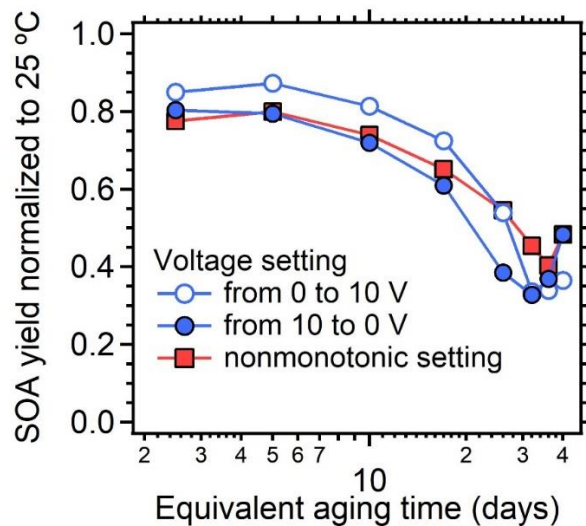
185 **Figure S20. Simulated ratio of SOA yield with measured temperature vs. that under 25 °C under varied lamp settings. A 10-ppb toluene with mass concentration of 30 μg m⁻³ of OA seed (inlet mass concentration) was assumed. The equivalent aging time was calculated by assuming the ambient OH concentration equated to 1.5×10^6 molecule cm⁻³ (Mao et al., 2009).**

References

Bianchi, F., Kurten, T., Riva, M., Mohr, C., Rissanen, M. P., Roldin, P., Berndt, T., Crounse, J. D., Wennberg, P. O., Mentel, T. F., Wildt, J., Junninen, H., Jokinen, T., Kulmala, M., Worsnop, D. R., Thornton, J. A., Donahue, N., Kjaergaard, H. G., and Ehn, M.: Highly Oxygenated Organic Molecules (HOM) from Gas-Phase Autoxidation Involving Peroxy Radicals: A Key Contributor to Atmospheric Aerosol, Chem Rev, 119, 3472-3509, https://doi.org/10.1021/acs.chemrev.8b00395, 2019.

Cappa, C. D., Zhang, X., Loza, C. L., Craven, J. S., Yee, L. D., and Seinfeld, J. H.: Application of the Statistical Oxidation Model (SOM) to Secondary Organic Aerosol formation from photooxidation of of C12 alkanes, Atmospheric Chemistry and Physics, 13, 1591-1606, https://doi.org/10.5194/acp-13-1591-2013, 2013.

Chhabra, P. S., Ng, N. L., Canagaratna, M. R., Corrigan, A. L., Russell, L. M., Worsnop, D. R., Flagan, R. C., and Seinfeld, J. H.: Elemental composition and oxidation of chamber organic aerosol, Atmospheric Chemistry and Physics, 11, 8827-8845, https://doi.org/10.5194/acp-11-8827-2011, 2011.

Epstein, S. A., Riipinen, I., and Donahue, N. M.: A semiempirical correlation between enthalpy of vaporization and saturation concentration for organic aerosol, Environ Sci Technol, 44, 743-748, https://doi.org/10.1021/es902497z, 2010.

Holman, J. P.: Heat Transfer, 10 edn, McGraw-Hill, New York, USA, 2010.

Hu, W., Zhou, H., Chen, W., Ye, Y., Pan, T., Wang, Y., Song, W., Zhang, H., Deng, W., Zhu, M., Wang, C., Wu, C., Ye, C., Wang, Z., Yuan, B., Huang, S., Shao, M., Peng, Z., Day, D. A., Campuzano-Jost, P., Lambe, A. T., Worsnop, D. R., Jimenez, J. L., and Wang, X.: Oxidation Flow Reactor Results in a Chinese Megacity Emphasize the Important Contribution of S/IVOCs to Ambient SOA Formation, Environ Sci Technol, 56, 6880-6893, https://doi.org/10.1021/acs.est.1c03155, 2022.

Huang, Y., Coggon, M. M., Zhao, R., Lignell, H., Bauer, M. U., Flagan, R. C., and Seinfeld, J. H.: The Caltech Photooxidation Flow Tube reactor: design, fluid dynamics and characterization, Atmospheric Measurement Techniques, 10, 839-867, https://doi.org/10.5194/amt-10-839-2017, 2017.

Loza, C. L., Craven, J. S., Yee, L. D., Coggon, M. M., Schwantes, R. H., Shiraiwa, M., Zhang, X., Schilling, K. A., Ng, N. L., Canagaratna, M. R., Ziemann, P. J., Flagan, R. C., and Seinfeld, J. H.: Secondary organic aerosol yields of 12-carbon alkanes, Atmospheric Chemistry and Physics, 14, 1423-1439, https://doi.org/10.5194/acp-14-1423-2014, 2014.

Mao, J., Ren, X., Brune, W. H., Olson, J. R., Crawford, J. H., Fried, A., Huey, L. G., Cohen, R. C., Heikes, B., Singh, H. B., Blake, D. R., Sachse, G. W., Diskin, G. S., Hall, S. R., and Shetter, R. E.: Airborne measurement of OH reactivity during INTEX-B, Atmospheric Chemistry and Physics, 9, 163-173, https://doi.org/10.5194/acp-9-163-2009, 2009.

Ng, N. L., Kroll, J. H., Chan, A. W. H., Chhabra, P. S., Flagan, R. C., and Seinfeld, J. H.: Secondary organic aerosol formation from m-xylene, toluene, and benzene, Atmospheric Chemistry and Physics, 7, 3909-3922, https://doi.org/10.5194/acp-7-3909-2007, 2007.

Peng, Z., Palm, B. B., Day, D. A., Talukdar, R. K., Hu, W., Lambe, A. T., Brune, W. H., and Jimenez, J. L.: Model Evaluation of New Techniques for Maintaining High-NO Conditions in Oxidation Flow Reactors for the Study of OH-Initiated Atmospheric Chemistry, ACS Earth and Space Chemistry, 2, 72-86, https://doi.org/10.1021/acsearthspacechem.7b00070, 2018.

Zhang, X., Cappa, C. D., Jathar, S. H., McVay, R. C., Ensberg, J. J., Kleeman, M. J., and Seinfeld, J. H.: Influence of vapor wall loss in laboratory chambers on yields of secondary organic aerosol, Proc Natl Acad Sci U S A, 111, 5802-5807, https://doi.org/10.1073/pnas.1404727111, 2014.